Desalination and Water Treatment
www.deswater.com
doi: 10.1080/19443994.2015.1099330

57 (2016) 23196–23205
October

Taylor & Francis
Taylor & Francis Group

Dynamic performance of vacuum membrane distillation system

Ashraf S. Hassan[a,b,*], Hassan E.S. Fath[c], Mohamed Darwish[a], Hassan Abdulrahim[a]

[a]*Desalination and Water Reuse, Qatar Environment and Energy Research Institute, Doha, Qatar, email: ahassan@qf.org.qa (A.S. Hassan), mdarwish@qf.org.qa (M. Darwish), habdelrehem@qf.org.qa (H. Abdulrahim)*
[b]*Planning and Following-up, Nuclear Power Plants Authority, Cairo, Egypt*
[c]*Mechanical Engineering Department, American University of Sharja, Sharja, UAE, email: hfath@aus.edu*

Received 5 April 2015; Accepted 13 August 2015

ABSTRACT

The aim of this work was the development of a numerical methodology to simulate and study the dynamic behavior of vacuum membrane distillation (VMD) system. A time-dependent one-dimensional finite difference numerical model is developed to study the flow as well as thermal regimes and the dynamic operational performance of VMD under stepped flow disturbance function in the hot channel. The study simulates the process parameters including mass flow rates, temperatures, vapor pressures, and concentration distributions for the hot feed channels along the flat-plate membrane length with transmembrane flux. The developed dynamic tool predicts the hydrodynamic behaviors and thermal characteristics of the very thin channels of VMD module. A rectangular pulse disturbance function is applied to rise up the inlet hot mass flow rate from steady state (SS) value of 1 to 1.34 kg/s for 60 s. The model ran for 3 min, which included the 60 s of applied dynamic disturbance; it started at the 10th s and finished at the 70th s. The results show that the probability of the pressure rise and the salt precipitation (scaling problem) will appear on the second half of the membrane length more than on the first half. The hydrodynamic influence of the flow conditions on the permeate flux appears to be more significant at the feed side of the VMD module fillet.

Keywords: Vacuum membrane distillation; Transient performance; Dynamic modeling; Desalination

1. Introduction

Conventional membrane processes, in general, are very attractive because of their simplicity and flexibility. Their basic properties make them ideal for application in the production of high quality fruit juices. They generally use gentle temperatures during the operation and do not involve phase changes or chemical additives. They are also characterized by low specific energy consumption [1].

As one of the potential solutions for freshwater recovery from high salinity brines, membrane distillation (MD) has shown promising prospects with the utilization of low-grade thermal energy [2,3]. MD process

*Corresponding author.

Presented at EuroMed 2015: Desalination for Clean Water and Energy Palermo, Italy, 10–14 May 2015. Organized by the European Desalination Society

is an integrated thermal/membrane desalination process in which pure water vapor from a salty solution passes through a hydrophobic membrane, driven by temperature across membrane, and condenses on the opposite side of the membrane. In MD, the vapor transport occurs in three steps: (i) evaporation from the hot liquid feed concentrate, (ii) vapor transport through the porous membrane, and (iii) condensation to a cold liquid permeate. The temperature difference across the two sides of the hydrophobic membrane leads to a partial pressure difference that causes water to evaporate and vapor transport. Due to high surface tension of the polymeric membrane materials, liquid water is prevented from entering the membrane pores, while molecular water in the vapor phase can pass through.

The MD process can generally be subdivided into four different types, Fig. 1, direct contact membrane distillation (DCMD), air gap membrane distillation (AGMD), sweeping gas membrane distillation (SGMD), and vacuum membrane distillation (VMD). Most of these technologies have been tested either in laboratory bench-scale or in small-scale pilot test units.

Alsaadi et al. [4] mentioned that the concentration polarization takes place in both isothermal processes (e.g. reverse osmosis and forward osmosis), and in non-isothermal processes (e.g. MD). Temperature polarization develops only in non-isothermal processes and results in a reduction of the driving force of the permeate flux when a thermal gradient is formed near the membrane surface. Khalifa [5] presented a theoretical model of liquid air gap MD and observed that the vapor mass flux increases by increasing flow rate (both feed and coolant), feed solution temperature, and the membrane length.

The hydrodynamic behaviors of the pressure drop and heat transfer characteristics of very thin (in millimeters) channels of MD module are very important for industry. Knowledge of the performance of MD thin-channel or micro-channels in laminar, transitional, and turbulent flow regimes are very vital to ensure thermally effective and energy efficient MD system. Investigations of micro-channel was revised by Dirker et al. [6] with a range of contradicting published results (in terms of friction factor and Nusselt number) as compared to conventional macro-channels behavior.

2. VMD theory and process description

VMD has recently shown a greater interest in desalination and food industries. The dynamic behavior of the VMD system is important for many industrial system operation. This paper addresses, therefore, the VMD dynamic performance. The mass transport in VMD contains phase change from liquid to vapor phase. The liquid feed side is in contact with the porous composite hydrophobic/hydrophilic membrane, where the hydrophobic membrane is the active layer and the hydrophilic membrane is the support layer. The vacuum is applied on the permeate side of the membrane. The pressure difference between the vacuum side and the pressurized feed side creates the driving force for the mass transport in VMD. The permeate, in vapor phase inside the membrane module, will condense in the vacuum side, however, outside the membrane zone. Depending on the process conditions and membrane characteristics, the mass transport can be described by Knudsen diffusion, Poisseuille flow, and molecular diffusion or their combination [7–9].

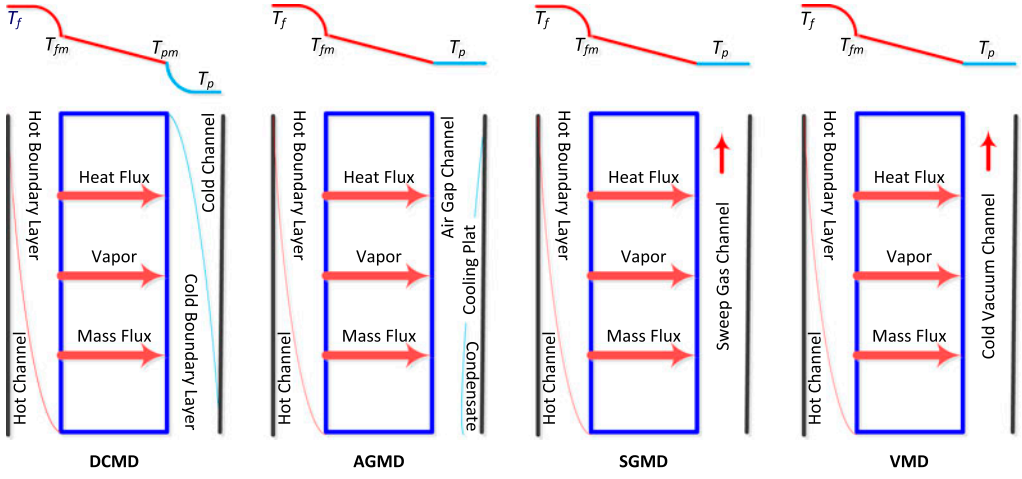

Fig. 1. Different types of the MD configurations.

VMD system consists of a VMD module feeding with slightly pressurized hot saline water. The permeate vapor passes through the hydrophobic membrane and the rejected brine gets out of the membrane at higher concentration. On the other side of the membrane, the saturation pressure is transported by vacuum pump passing through a condenser, Fig. 2(a). A simultaneous mass and heat transfer through a flat-plate membrane occurs during the VMD process, where the mass transfer takes place in the transported vapor, while the heat is transferred through both the transported vapor and the membrane, Fig. 2(b).

3. Governing equations and solution

3.1. Introduction

A transient dynamic model has been developed for the VMD desalination system. The model simulates VMD process parameters including mass flow rate, temperature, pressure, and concentration distributions for hot feed channels along the membrane length with permeate flux for a typical commercial flat-plate membrane system. The SS model is first built with FORTRAN language. To numerically solve the set of the governing partial differential equations, the steady state (SS) results are, then, used as initial values in the dynamic model that used Berkeley Madonna modeling tool.

3.2. General equations

The transient one-dimensional (x-direction) governing equations for hot channel of the VMD module and transmembrane flux through the membrane thickness can be determined as follows:

$$\text{Continuity equation: } \frac{\partial \rho}{\partial t} + \frac{\partial(\rho u)}{\partial x} = 0 \tag{1}$$

$$\text{Momentum equations: } \frac{\partial(\rho u)}{\partial t} + u\frac{\partial(\rho u)}{\partial x} = -\frac{\partial P}{\partial x} + \mu\frac{\partial^2 u}{\partial x^2} \tag{2}$$

$$\text{Energy equation: } C_P\left(\frac{\partial(\rho T)}{\partial t} + u\frac{\partial(\rho T)}{\partial x}\right) = k\frac{\partial^2 T}{\partial x^2} \tag{3}$$

$$\text{Species equation: } \frac{\partial C}{\partial t} + u\frac{\partial C}{\partial x} = D\frac{\partial^2 C}{\partial x^2} \tag{4}$$

$$\text{Transmembrane mass flux equation: } \frac{\partial}{\partial t}J_m(x) = C_m\frac{\partial}{\partial t}\left(P_{f,m}(x) - P_{vac}\right) \tag{5}$$

For laminar flow, the value of the Reynolds (Re) number must be less than approximately 2,100 and greater than 4,000 for turbulent flow [10]. For turbulent flow, the frictional factor (f) Eq. (6) [11], is used to calculate the turbulent flow Nusselt (Nu) number Eq. (7) [6]. For laminar flow, Nu can be expressed as given in Eq. (8). Using Newton's law of cooling, the local convection heat transfer coefficient (H_f) can be expressed as given in Eq. (9).

$$f = 0.0791\,Re^{-0.25} \tag{6}$$

$$Nu_f = \frac{0.125f(Re - 1000)Pr}{1 + 12.7(0.125f)^{0.5}(Pr^{2/3} - 1)}, \quad \text{for turblent flow} \tag{7}$$

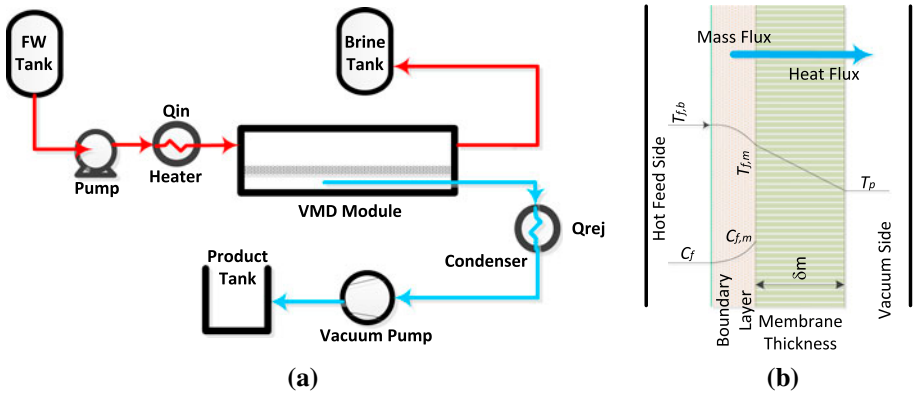

Fig. 2. (a) Process flow diagram of VMD system and (b) physical model of VMD module.

$$Nu_f = 7.54 + \frac{0.03\,Re\,Pr\,d_h/L}{1 + 0.016(Re\,Pr\,d_h/L)^{2/3}}, \quad \text{for laminar flow} \tag{8}$$

$$H_f = \frac{Nu\,k_f}{d_h} \tag{9}$$

The thermal conductivity (K_m) of the membrane can be predicted using Eq. (10) [12], where K_s and K_g are the thermal conductivities of the membrane polymer and air/gas, respectively, while ε is the porosity of the membrane.

$$K_m = K_s\,(1 - \varepsilon) + \varepsilon K_g \tag{10}$$

3.3. Assumptions

The feed flow rate is taken as 1.0 kg/s, feed temperature is 85°C, vacuum pressure is 0.0317 bar, membrane length 10 m, membrane width 0.5 m, height of hot channel is 0.004 m, membrane coefficient is 1.6×10^{-7} kg/s m^2 Pa, and feed water salinity is 45,000 ppm.

The flow in hot channel is simulated as one-dimensional coordinate. The active length is divided into 50 cells and the physical properties and operating parameters at each cell are calculated. The mesh (cell) is in x-direction along the membrane length (L). The governing partial differential equations of mass, momentum, and energy conservations, are solved for each cell.

A typical rectangular pulse forcing (or disturbance) function is applied to rise up the inlet hot mass flow rate from steady state (SS) value of 1.0 to 1.34 kg/s for 60 s, then return to SS value once again. The model ran for 3 min, which included one minute of applied dynamic disturbance; it started at the 10th second and finished at the 70th second.

3.4. Code verification

Fig. 3(a) and (b) shows a comparison between model's results and the published results by Imdakm et al. [13], for different feed water temperatures. Applied Monte Carlo simulation model is used to describe VMD process performance. The present and publish results are in good assumption and show that VMD flux decreases quite linearly with the increase in the downstream up to the bulk feed vapor pressure, P_f, and for higher bulk feed temperature.

4. Results and discussion

Fig. 4 shows the hydrodynamic behavior for the hot feed mass flow rate where a sharp rectangular pulse took place in cell #1 from time 10 to 70 s. Each line represents the behavior of the studied mass flow rate for each cell (from 1 to 50) along the membrane length. The arrow plotted in the figure, indicates the trend of the change in values for all cells from 1 to 50. The pulse in the cells along the membrane length (cells 2–50) decreased gradually as compared to flow pulse signals with smooth reactions (no sharp changes). This behavior is a stable response because the disturbance action emerged, and lasted around the forcing time then returned to the initial SS value once again; cell # 1 started the pulse disturbance at 10 s and finished at 70 s, while cell # 50 (10 m far from cell # 1) started at about 50 s and finished at about 140 s.

Any increase in the saturated water vapor pressure at the liquid/vapor interface will increase the driving force for water vapor permeation across the membrane, resulting in an increase in the permeation flux [14]. This result is very clear, in Figs. 5(a) and 6(b), in case of decreasing the membrane surface pressure ($P_{f,m}$) inside the hot channel along the membrane length, Fig. 5(a) illustrates the SS response of the $P_{f,m}$ along the membrane length in x-direction. Due to the behavior of the hot channel, by the forcing function on the feed flow rate, the response of $P_{f,m}$ gradually increased during the disturbance period then decreased and was maintained constant at the SS value, as shown in Fig. 5(b). There is no change in the pressure of the inlet feed, while the $P_{f,m}$ will follow the behavior of feed flow rate inside and along the length of the VMD module. The difference between dynamic behavior of the $P_{f,m}$ for each cell along the membrane length at different selected times (30, 50 70, 90, and 110 s) and the SS value of each cell are show in Fig. 5(c). For the 70th second, the end of the disturbance action, the pressure difference quickly increased to reach the maximum difference value at 0.5 L, then slowly decreased until the end of the membrane. As a result, the first half of the membrane length will not face any severe change in pressure, while the second half length will face the highest value of the pressure change.

Eq. (5) represents the partial differential equation of the transmembrane mass flux (J_m) along the membrane length for ith cell. The influence of the pressure conditions on the permeate flux is more significant at the VMD module. Therefore, the time dependent response of the permeate flux is affected by the response of the pressure on the two sides of the

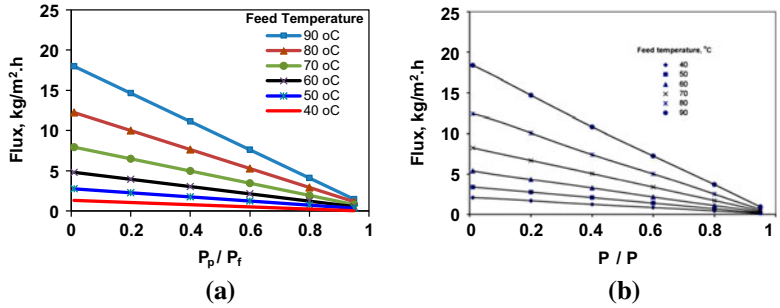

Fig. 3. Compare model's results (a) with the published results and (b) of Ref. [13].

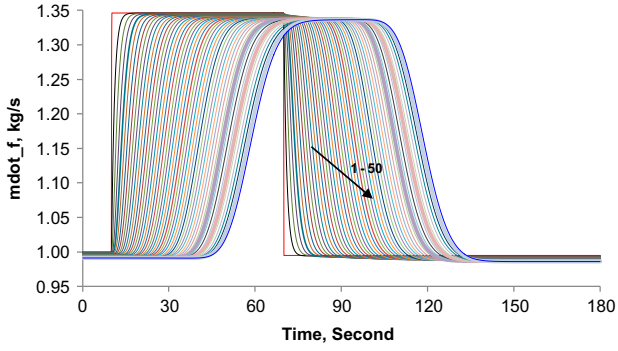

Fig. 4. The hydrodynamic behavior of the mass flow rate along the module length.

membrane surfaces, i.e. $P_{f,m}$ and vacuum pressure (P_{vac}). For simplicity, the characteristic membrane coefficient (C_m) is assumed independent of the changes in temperature and time parameters. Fig. 6(a) represents the time response of the permeate flux along the membrane length due to the system disturbance. Although, the transport of the permeate flux decreased along the membrane length, in the SS model Fig. 6(b), the time behavior of the integration of the permeate flux (the production) will smoothly increase during the disturbance duration, then bound to the initial SS values, as shown in Fig. 6(c). Indeed, the change of the transmembrane flux along the membrane length follows the change of feed pressure on the membrane surface. Therefore, the trend of the difference between

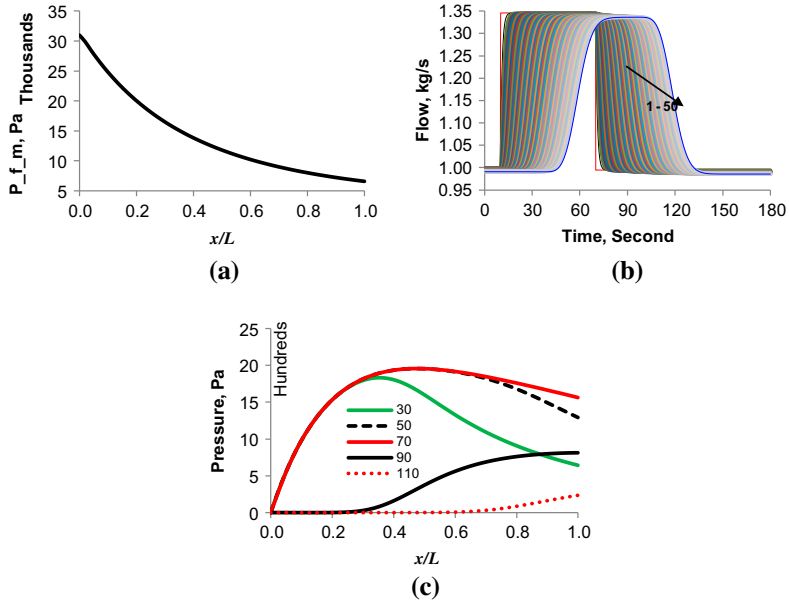

Fig. 5. (a) SS model of pressure variation along the membrane length, (b) dynamic behavior of the membrane surface pressure, and (c) pressure difference between the response of the time line (30, 50 70, 90, and 110 s) and SS value.

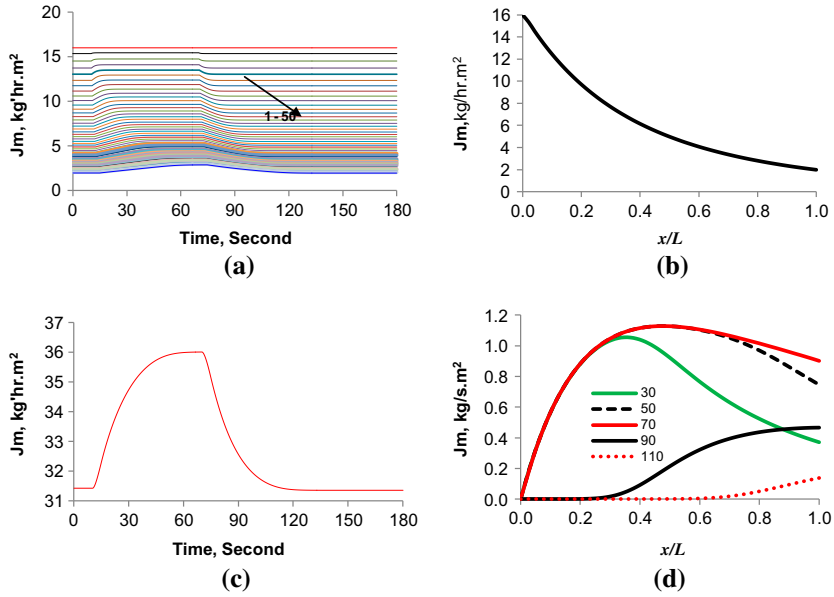

Fig. 6. (a) Dynamic behavior of the transmembrane flux, (b) SS permeate flux variation along the membrane length, (c) behavior of flux production, and (d) difference between the response of the time line of the transmembrane flux (30, 50 70, 90 and 110 s) and SS value.

dynamic behavior of permeate flux for each cell at different selected times and the SS value of each cell, shown in Fig. 6(d), will be matched with the trend of the pressure change in Fig. 5(c).

At the surface of the membrane, a hot liquid evaporates and the water vapor (latent heat—h_{fg}) is transferred across the membrane at heat flux rate q_{out} into vacuum space. Eq. (11) determines the heat flux by conduction across the membrane (q_m). To simplify, the temperature dependence for membrane thermal conductivity is addressed here. The total heat flux (q_{out}), Eq. (12), transferred across the membrane from hot channel into the vacuum space can be calculated as a function of the latent heat of the bulk feed flow ($h_{fg,b}$) and the latent heat on the membrane surface ($h_{fg,m}$).

$$\frac{\partial}{\partial t} q_m(i) = K_{\text{cond}} \frac{\partial}{\partial t} \left(T_{f,m}(i) - T_P \right) \tag{11}$$

$$\frac{\partial}{\partial t} q_{\text{out}}(i) = \frac{\partial}{\partial t} \left(J_m(i) h_{fg,f}(i) \right) + \frac{\partial}{\partial t} q_m(i) - \frac{\partial}{\partial t} \left(J_m(i) \left(h_{f,b}(i) - h_{f,m}(i) \right) \right) \tag{12}$$

In VMD, both the thermal boundary layer resistance on the permeate side and the participation of conductive heat transfer across the membrane matrix are poor, owing to low pressure applied to the permeate side of the membrane [15]. The value of bulk feed temperature ($T_{f,b}$) can easily be measured, but the membrane surface temperature ($T_{f,m}$) cannot. It could be calculated mathematically via an enthalpy balance. The pressure profiles, shown in Fig. 5, the thermal properties distributions shown in Figs. 7, 8, and Fig. 9 shows the significant influence on the dynamic behavior along the membrane length for $T_{f,b}$, $T_{f,m}$, h_{fg}, and q_{out}, respectively. Before the end of the disturbance function at the 70th, the local changes in temperatures of $T_{f,b}$ (Fig. 7(c)) and $T_{f,m}$ (Fig. 7(d)), increased quickly compared with the SS values, to reach maximum difference values along the membrane length. While, the changes after the disturbance time increased slowly in the first half of the length of the membrane, then grew fast.

$$\frac{\partial}{\partial t} T_{f,m}(i) = \frac{\partial}{\partial t} T_{f,b}(i) - \frac{1}{H_f} \frac{\partial}{\partial t} q_{\text{out}}(i) \tag{13}$$

$$\frac{\partial}{\partial t} h_{f,m}(i) = 4210.8 \frac{\partial}{\partial t} T_{f,m}(i) - 1.24 T_{f,m}(i) \frac{\partial}{\partial t} T_{f,m}(i) + 0.0134 T_{f,m}(i) \frac{\partial}{\partial t} T_{f,m}(i) \tag{14}$$

$$\frac{\partial}{\partial t} h_{f,b}(i+1) = \frac{\partial}{\partial t} h_{f,b}(i) - dA \frac{\partial}{\partial t} \left(\frac{q_{\text{out}}(i)}{m_f(i)} \right) \tag{15}$$

$$\frac{\partial}{\partial t} \text{TPC}(i) = \frac{\partial}{\partial t} \left(\frac{T_{f,m}(i)}{T_{f,b}(i)} \right) \tag{16}$$

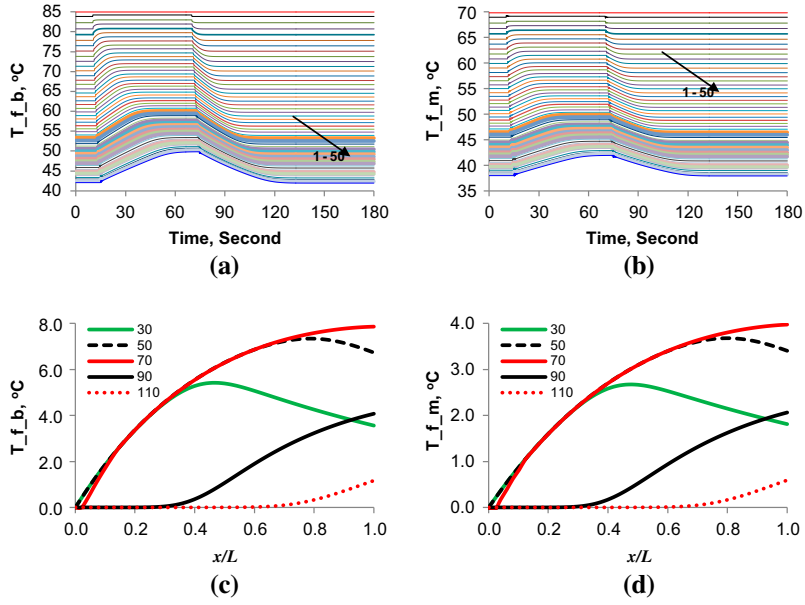

Fig. 7. Dynamic behavior for (a) feed water bulk local temperature, (b) membrane surface temperature, the temperature difference between the response of the time line, (c) at bulk feed water temperature, and (d) at surface membrane temperature (30, 50 70, 90, and 110 s), and SS value.

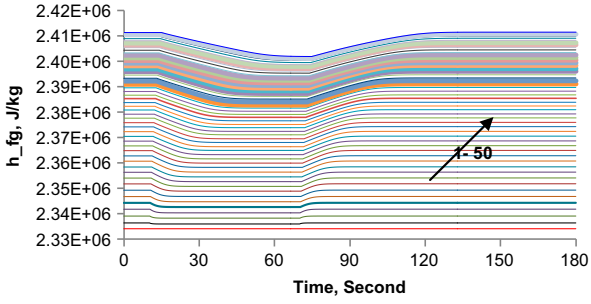

Fig. 8. Dynamic behavior of the feed flow latent heat.

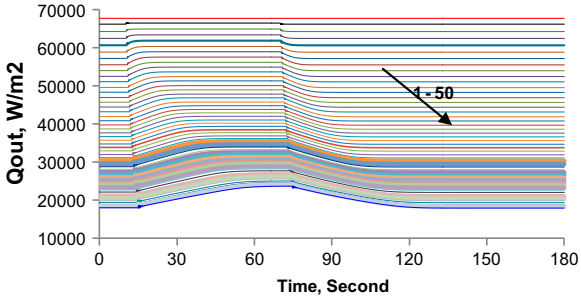

Fig. 9. Dynamic behavior of transported heat flux through the membrane.

$$\frac{\partial}{\partial t}\mathrm{CPC}(i) = \frac{1}{S_{f,in}}\frac{\partial}{\partial t}S_{f,b}(i) \tag{17}$$

$$\frac{\partial}{\partial t}S_f(i) = \frac{\partial}{\partial t}\left(\frac{m_f(i-1)S_f(i-1)}{m_f(i-1)-\delta_A J_m(i)}\right) \tag{18}$$

The time dependent, Eq. (18), of feed water salinity (S_f) represents the behavior flow concentration along the membrane length following the time response of the hot channel flow rate and the permeate flux transported through each cell area (δ_A) along the membrane length. Fig. 10(a) presents the time behavior, during the disturbance period, in flow concentration, while Fig. 10(b) shows, along x-direction, the variation in the concentration calculated via SS model. To understand the changes between the dynamic behavior of the salt concentration and the SS values along the membrane length, as shown in the Fig. 10(c), it is necessary to look at Figs. 6(d) and 10(d), where the changes in transmembrane flux are not the same as the changes in feed water flow rates along the membrane length. This indicates that the probability of salt precipitation or scaling problem will appear on the second half of the membrane length.

The feed flow hydrodynamic and the feed concentration are two important factors that influence the mass transfer resistance in the liquid boundary layer.

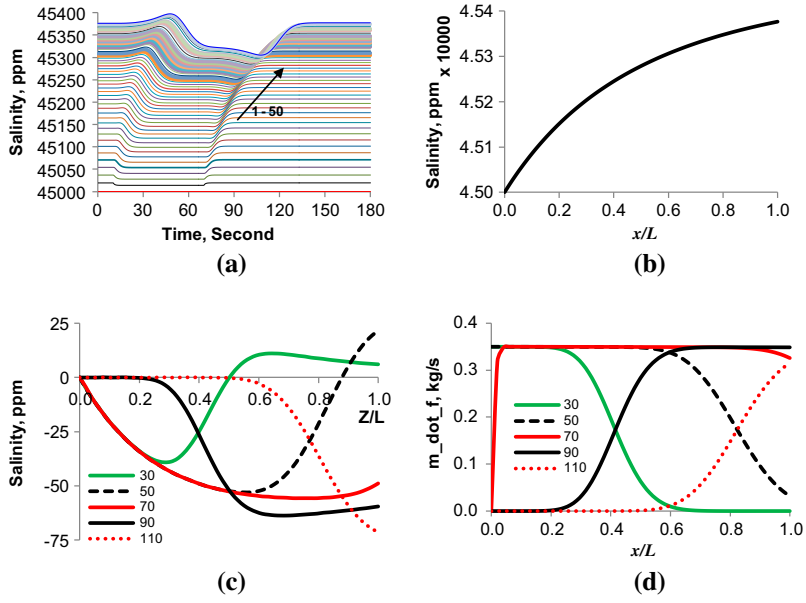

Fig. 10. (a) Dynamic behavior of flow salinity, (b) the SS concentration variation in *x*-direction, (c) the concentration difference between the response of the time line and SS value, and (d) difference between the behavior of the feed water flow rate (30, 50 70, 90, and 110 s) and SS value.

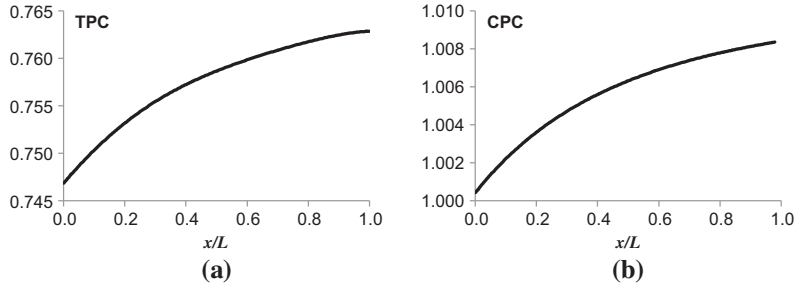

Fig. 11. Variation of SS results along the membrane length for: (a) TPC and (b) CPC.

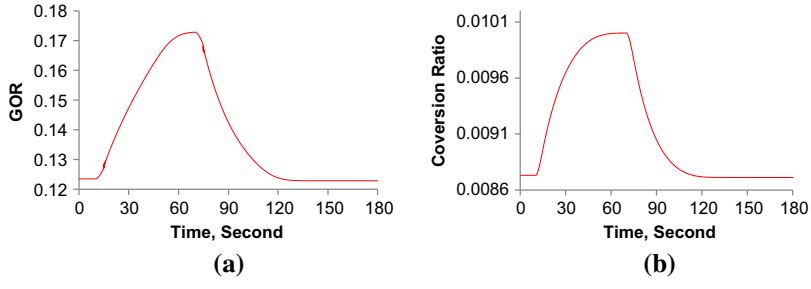

Fig. 12. Dynamic behavior for (a) GOR and (b) CR.

The partial deferential equation of temperature polarization coefficient (TPC) can be mathematically driven as formed in Eq. (16), in which the numerical values of TPC should be equal or less than unity. Fig. 11(a) shows the variation of TPC in x-direction. The time dependence of the concentration polarization coefficient (CPC) can be determined using Eq. (17). As shown in Fig. 11(b), CPC should be greater than unity.

The transport model is to be established to correlate the local permeation rate with the overall VMD module performance. Therefore, the time behavior of the VMD system performance can be determined via gain output ratio (GOR) or the conversion ratio (CR). Eqs. (19) and (20) show the dynamic behavior of the *GOR* and CR, respectively, for VMD system. Clearly, the influence of the flow conditions on the permeate flux is more significant at the feed side of the VMD module (Fig. 12).

$$\frac{\partial}{\partial t}\mathrm{GOR} = \frac{\partial}{\partial t}\left(\frac{m_p h_p}{q_{in}}\right) \tag{19}$$

$$\frac{\partial}{\partial t}\mathrm{CR} = \frac{\partial}{\partial t}\left(\frac{m_p}{m_{f,in}}\right) \tag{20}$$

5. Conclusion

A dynamic tool was developed to predict the hydrodynamic behaviors of the physical and thermal characteristics of very thin channels of VMD module. A good understanding of the performance of VMD system is very vital to ensure thermally effective and energy efficient operating system. The mathematical model of the dynamic behavior could simulate the real actions and reactions for the complicated arithmetic models. Although the forcing function applied on the inlet feed flow rate was a sharp rectangular pulse, the behavior of the other system parameters was gradually changed. The results show that hydrodynamic influence of the flow conditions on the permeate flux is more significant at the feed side of the VMD module. The probability of the pressure rise and the salt precipitation (scaling problem) will appear also on the second half of the membrane length more than on the first half.

Nomenclatures

AGMD — air gap membrane distillation
C — solute concentration
C_m — membrane permeability coefficient (kg/s m^2 Pa)
CPC — concentration polarization coefficient
CR — conversion ratio
D — diffusion coefficient
DCMD — direct contact membrane distillation
d_h — hydraulic diameter (m)
f — friction factor
GOR — gain output ratio
H — heat transfer coefficient (W/m^2 k)
h — enthalpy (J/kg)
J — permeate flux (kg/m^2 h)
K — thermal conductivity (W/m k)
k_{cond} — thermal conduction of the membrane
L — membrane length (m)
m — mass flow rate (kg/s)
Nu — Nusselt number
P — pressure (Pa)
Pr — Prandtl number
q — heat flux rate (W/m^2)
Re — Reynolds number
S — flow salinity (ppm)
SGMD — swept gas membrane distillation
T — temperature (°C)
TPC — temperature polarization coefficient
u — velocity vector in x-direction
VMD — vacuum membrane distillation

Greek letters

ε — membrane porosity (%)
Δ — difference
μ — dynamic viscosity
ρ — density
δ_A — cell area (m^2)
δ_m — membrane thickness (m)

Subscripts

b — bulk
f — feed or liquid
fg — latent heat
g — gas or air
m — membrane
s — solid
vac — vacuum

References

[1] N. Diban, O.C. Voinea, A. Urtiaga, I. Ortiz, Vacuum membrane distillation of the main pear aroma compound: Experimental study and mass transfer modeling, J. Membr. Sci. 326 (2009) 64–75.
[2] A.S. Hassan, H.E.S. Fath, Review and assessment of the newly developed MD for desalination processes, Desalin. Water Treat. 51(1–3) (2013) 574–585.
[3] G. Guan, X. Yang, R. Wang, R. Field, A.G. Fane, Evaluation of hollow fiber-based direct contact and vacuum membrane distillation systems using aspen process simulation, J. Membr. Sci. 464 (2014) 127–139.
[4] A.S. Alsaadi, L. Francis, G.L. Amy, N. Ghaffour, Experimental and theoretical analyses of temperature polarization effect in vacuum membrane distillation, J. Membr. Sci. 471 (2014) 138–148.

[5] A.E. Khalifa, Water and air gap membrane distillation for water desalination—An experimental comparative study, Sep. Purif. Technol. 141 (2015) 276–284.
[6] J. Dirker, J.P. Meyer, D.V. Garach, Inlet flow effects in micro-channels in the laminar and transitional regimes on single-phase heat transfer coefficients and friction factors, Int. J. Heat Mass Transfer 77 (2014) 612–626.
[7] A. Rom, W. Wukovits, F. Anton, Development of a vacuum membrane distillation unit operation: From experimental data to a simulation model, Chem. Eng. Process. 86 (2014) 90–95.
[8] K.W. Lawson, D.R. Lloyd, Review Membrane Distillation, J. Membr. Sci. 124 (1997) 1–25.
[9] K.W. Lawson, D.R. Lloyd, Membrane distillation, J. Membr. Sci. 124 (1997) 1–25.
[10] D.F. Young, B.R. Munson, T.H. Okiishi, W.W. Huebsch, Introduction to Fluid Mechanics, fifth ed., John Wiley & Sons, Hoboken, NJ, 2012.
[11] R.S. Vajjha, D.K. Das, D.R. Ray, Development of new correlations for the Nusselt number and the friction factor under turbulent flow of nanofluids in flat tubes, Int. J. Heat Mass Transfer 80 (2015) 353–367.
[12] I. Hitsov, T. Maere, K. De Sitter, C. Dotremont, I. Nopens, Modelling approaches in membrane distillation: A critical review, Sep. Purif. Technol. 142 (2015) 48–64.
[13] A.O. Imdakm, M. Khayet, T. Matsuura, A Monte Carlo simulation model for vacuum membrane distillation process, J. Membr. Sci. 306 (2007) 341–348.
[14] A.C. Sun, W. Kosar, Y. Zhang, X. Feng, Vacuum membrane distillation for desalination of water using hollow fiber membranes, J. Membr. Sci. 455 (2014) 131–142.
[15] M.A.E.-R. Abu-Zeid, Y. Zhang, H. Dong, L. Zhang, H.-L. Chen, L. Hou, A comprehensive review of vacuum membrane distillation technique, Desalination 356 (2015) 1–14.